

KMT-2018-BLG-0029Lb: A VERY LOW MASS-RATIO *Spitzer* MICROLENS PLANET

ANDREW GOULD^{1,2}, YOON-HYUN RYU³, SEBASTIANO CALCHI NOVATI⁴, WEICHENG ZANG⁵,
AND

¹, MICHAEL D. ALBROW⁶, SUN-JU CHUNG^{3,7}, CHEONGHO HAN⁸, KYU-HA HWANG³, YOUNG KIL JUNG³, IN-GU SHIN³,
YOSSI SHVARTZVALD⁹, JENNIFER C. YEE¹⁰, SANG-MOK CHA^{3,11}, DONG-JIN KIM³, HYOUN-WOO KIM³, SEUNG-LEE
KIM^{3,7}, CHUNG-UK LEE^{3,7}, DONG-JOO LEE³, YONGSEOK LEE^{3,11}, BYEONG-GON PARK^{3,7}, RICHARD W. POGGE²,
(KMTNET COLLABORATION)
¹, CHARLES BEICHMAN¹², GEOFF BRYDEN⁹, SEAN CAREY¹³, B. SCOTT GAUDI², CALEN B. HENDERSON⁹, WEI ZHU¹⁴,
(*Spitzer* TEAM)
¹, PASCAL FOUQUÉ^{15,16}, MATTHEW T. PENNY², ANDREEA PETRIC¹⁵, TODD BURDULLIS¹⁵, SHUDE MAO^{17,18},
(CFHT MICROLENSING COLLABORATION)

¹Max-Planck-Institute for Astronomy, Königstuhl 17, 69117 Heidelberg, Germany

²Department of Astronomy Ohio State University, 140 W. 18th Ave., Columbus, OH 43210, USA

³Korea Astronomy and Space Science Institute, Daejeon 34055, Republic of Korea

⁴IPAC, Mail Code 100-22, Caltech, 1200 E. California Blvd., Pasadena, CA 91125, USA

⁵Physics Department and Tsinghua Centre for Astrophysics, Tsinghua University, Beijing 100084, China

⁶University of Canterbury, Department of Physics and Astronomy, Private Bag 4800, Christchurch 8020, New Zealand

⁷University of Science and Technology, Korea (UST) Gajeong-ro, Yuseong-gu, Daejeon 34113, Republic of Korea

⁸Department of Physics, Chungbuk National University, Cheongju 28644, Republic of Korea

⁹IPAC, Mail Code 100-22, Caltech, 1200 E. California Blvd., Pasadena, CA 91125, USA

¹⁰Center for Astrophysics | Harvard & Smithsonian, 60 Garden St., Cambridge, MA 02138, USA

¹¹School of Space Research, Kyung Hee University, Yongin, Gyeonggi 17104, Republic of Korea

¹²NASA Exoplanet Science Institute, California Institute of Technology, Pasadena, CA 91125, USA

¹³*Spitzer*, Science Center, MS 220-6, California Institute of Technology, Pasadena, CA, USA

¹⁴Canadian Institute for Theoretical Astrophysics, University of Toronto, 60 St George Street, Toronto, ON M5S 3H8,
Canada

¹⁵CFHT Corporation, 65-1238 Mamalahoa Hwy, Kamuela, Hawaii 96743, USA

¹⁶Université de Toulouse, UPS-OMP, IRAP, Toulouse, France

¹⁷Department of Astronomy and Tsinghua Centre for Astrophysics, Tsinghua University, Beijing 100084, China

¹⁸National Astronomical Observatories, Chinese Academy of Sciences, Beijing 100101, China

Received —; accepted —

Abstract: At $q = 1.81 \pm 0.20 \times 10^{-5}$, KMT-2018-BLG-0029Lb has the lowest planet-host mass ratio q of any microlensing planet to date by more than a factor of two. Hence, it is the first planet that probes below the apparent “pile-up” at $q = 5\text{--}10 \times 10^{-5}$. The event was observed by *Spitzer*, yielding a microlens-parallax π_E measurement. Combined with a measurement of the Einstein radius θ_E from finite-source effects during the caustic crossings, these measurements imply masses of the host $M_{\text{host}} = 1.06^{+0.20}_{-0.17} M_{\odot}$ and planet $M_{\text{planet}} = 6.41^{+0.89}_{-0.75} M_{\oplus}$, system distance $D_L = 2.73^{+0.26}_{-0.22}$ kpc and projected separation $a_{\perp} = 3.94^{+0.35}_{-0.31}$ AU.

Key words: gravitational microlensing; micro; planetary systems

1. INTRODUCTION

For most microlensing planets, the planet-host mass ratio q is well determined, but the mass of the host, which is generally too faint to be reliably detected, remains unknown. Hence the planet mass also remains unknown. One way to carry out statistical studies in the face of this difficulty is to focus attention on the mass ratios themselves. Suzuki et al. (2016) conducted such a study, finding a break in the mass-ratio function at $q_{\text{br}} \sim 1.7 \times 10^{-4}$ based on planets detected in the MOA-II survey. Udalski et al. (2018) applied a V/V_{max}

technique to the seven then-known microlensing planets with well measured $q < 10^{-4}$ and confirmed that the slope of the mass-ratio function declines with decreasing mass ratio in this regime. Jung et al. (2019) considered all planets with $q < 3 \times 10^{-4}$ and concluded that if the mass-ratio function is treated as a broken power law, then the break is at $q_{\text{br}} \simeq 0.56 \times 10^{-4}$, with a change in the power-law index of $\zeta > 1.6$ at 2σ . However, they also noted that there were no detected microlensing planets with $q < 0.5 \times 10^{-4}$ and suggested that the low end of the mass-ratio function might be better characterized by a “pile-up” around $q \sim 0.7 \times 10^{-4}$ rather than a power-law break.

In principle, one might worry that the paucity of detected microlensing planets for $q \lesssim 0.5 \times 10^{-4}$ could be due to poor sensitivity at these mass ratios, which might then be overestimated in statistical studies. However, the detailed examination by Udalski et al. (2018) showed several planetary events would have been detected even with much lower mass ratios. In particular, they showed that OGLE-2017-BLG-1434Lb would have been detected down to $q = 0.018 \times 10^{-4}$ and that OGLE-2005-BLG-169Lb would have been detected down to $q = 0.063 \times 10^{-4}$. Hence, the lack of detected planets $q \lesssim 0.5 \times 10^{-4}$ remains a puzzle.

A substantial subset of microlensing planets, albeit a minority, do have host-mass determinations. For most of these the mass is determined by combining measurements of the Einstein radius θ_E and the microlens parallax π_E (Gould, 1992, 2000),

$$M = \frac{\theta_E}{\kappa \pi_E}; \quad \pi_{\text{rel}} = \theta_E \pi_E; \quad \kappa \equiv \frac{4G}{c^2 \text{AU}} \simeq 8.1 \frac{\text{mas}}{M_\odot}, \quad (1)$$

where

$$\theta_E = \sqrt{\kappa M \pi_{\text{rel}}}; \quad \pi_E = \frac{\pi_{\text{rel}}}{\theta_E} \frac{\mu_{\text{rel}}}{\mu_{\text{rel}}}, \quad (2)$$

and π_{rel} and μ_{rel} are the lens-source relative parallax and proper motion, respectively. While θ_E is routinely measured for caustic-crossing planetary events (the great majority of those published to date), π_E usually requires significant light-curve distortions induced by deviations from rectilinear lens-source relative motion caused by Earth’s annual motion. Thus, either the event must be unusually long or the parallax parameter $\pi_E = \sqrt{\pi_{\text{rel}}/\kappa M}$ must be unusually big. These criteria generally bias the sample to nearby lenses, e.g., OGLE-2006-BLG-109Lb,c (Gaudi et al., 2008; Bennett et al., 2010), which were the first two microlens planets with a clear parallax measurement. In a few cases, the host mass has been measured by direct detection of its light (Bennett et al., 2006, 2015; Batista et al., 2014, 2015). These measurements are also somewhat biased toward nearby lenses, although the main issue is that the lenses are typically much fainter than the sources, so that one must wait many years for the two to separate sufficiently on the plane of the sky to make useful observations.

Space-based microlens parallaxes (Refsdal, 1966; Gould, 1994; Dong et al., 2007) provide a powerful alternative, which is far less biased toward nearby lenses. Since 2014, *Spitzer* has observed almost 800 microlensing events toward the Galactic bulge (Gould et al., 2013, 2014, 2015a,b, 2016) with the principal aim of measuring the Galactic distribution of planets. In order to construct a valid statistical sample, Yee et al. (2015) established detailed protocols that govern the selection and observational cadence of these microlensing targets.

For 2014–2018, the overwhelming majority of targets were provided by the Optical Gravitational Lensing Experiment (OGLE, Udalski et al. 2015b) Early Warning System (EWS, Udalski et al. 1994; Udalski 2003), with approximately 6% provided by the Microlensing

Observations for Astrophysics (MOA, Bond et al. 2004) collaboration. In June 2018, the Korea Microlensing Telescope Network (KMTNet Kim et al. 2016) initiated a pilot alert program, covering about a third of its fields (Kim et al., 2018d). In order to maximize support for *Spitzer* microlensing, these fields were chosen to be in the northern Galactic bulge, which is relatively disfavored by microlensing surveys due to higher extinction, an effect that hardly impacts *Spitzer* observations at $3.6 \mu\text{m}$. This pilot program contributed about 17% of all 2018 *Spitzer* alerts. None of these events had obvious planetary signatures in the original online pipeline reductions. However, after the re-reduction of all 2018 KMT-discovered events (including those found by the post-season completed-event algorithm, Kim et al. 2018a), one of these *Spitzer* alerts, KMT-2018-BLG-0029, showed a hint of an anomaly in the light curve. This triggered tender loving care (TLC) re-reductions, which then revealed a clear planetary candidate.

The lens system has the lowest planet-host mass ratio $q = 0.18 \times 10^{-4}$ of any microlensing planet found to date by more than a factor of two.

2. OBSERVATIONS

2.1. KMT Observations

KMT-2018-BLG-0029 is at (RA,Dec) = (17:37:52.67, $-27:59:04.92$), corresponding to $(l, b) = (-0.09, +1.95)$. It lies in KMT field BLG14, which is observed by KMTNet with a nominal cadence of $\Gamma = 1.0 \text{ hr}^{-1}$ from its three sites at CTIO (KMTC), SAAO (KMTS), and SSO (KMTA) using three identical 1.6m telescopes, each equipped with a 4 deg^2 camera. The nominal cadence is maintained for all three telescopes during the “*Spitzer* season” (which formally began for 2018 on $\text{HJD}' = \text{HJD} - 2450000 = 8294.7$). But prior to this date, the cadence at KMTA and KMTS was at the reduced rate of $\Gamma = 0.75 \text{ hr}^{-1}$. The change to higher cadence fortuitously occurred just a few hours before the start of the KMTA observations of the anomaly.

The event was discovered on 30 May 2018 during “live testing” of the alert-finder algorithm, and was not publicly released until 21 June. However, as part of the test process, this (and all) alerts were made available to the *Spitzer* team (see Section 2.2, below).

The great majority of observations were carried out in the *I* band, but every tenth such observation is followed by a *V*-band observation that is made primarily to determine source colors. All reductions for the light curve analysis were conducted using pySIS (Albrow et al., 2009), which is a specific implementation of difference image analysis (DIA, Alard & Lupton 1998).

2.2. Spitzer Observations

The event was chosen by the *Spitzer* microlensing team at UT 23:21 on 19 June ($\text{JD}' = 8289.47$). The observational cadence was specified as “priority 1” (observe once per cycle of *Spitzer*-microlensing time) for the first

two weeks and “priority 2” (every other cycle) thereafter. Because the target lies well toward the western side of the microlensing fields, it was one of the relatively few events that were within the *Spitzer* viewing zone during the beginning of the *Spitzer* season. Therefore, it was observed (5, 4, 2, 2) times on (1, 2, 3, 4) July, compared to roughly one time per day for “priority 1” targets during the main part of the *Spitzer* season.

We note that the event was chosen by the *Spitzer* team about five days prior to the anomaly. However, as mentioned in Section 1, the anomaly could not be discerned from the on-line reduction in any case. The planet KMT-2018-BLG-0029 will therefore be part of the *Spitzer* microlensing statistical sample (Yee et al., 2015).

The *Spitzer* data were reduced using customized software that was written for the *Spitzer* microlensing program (Calchi Novati et al., 2015).

2.3. SMARTS ANDICAM Observations

The great majority of *Spitzer* events, particularly those in regions of relatively high extinction, are targeted for I/H observations using the ANDICAM dual-mode camera (DePoy et al., 2003) mounted on the SMARTS 1.3m telescope at CTIO. The purpose of these observations is to measure the source color, which is needed both to measure the angular radius of the source (Yoo et al., 2004) and to facilitate a color-color constraint on the *Spitzer* source flux (Yee et al., 2015; Calchi Novati et al., 2015). For this purpose, of order a half-dozen observations are usually made at a range of magnifications. Indeed, five such measurements were made of KMT-2018-BLG-0029. Each H -band observation is split into five 50-second dithered exposures.

The 2018 H -band observations did not extend to (or even near) baseline in part because the event is long but mainly because of engineering problems at the telescope late in the 2018 season. Hence, these data cover a range of magnification $12 \lesssim A \lesssim 33$. We therefore obtained six additional H -band epochs very near baseline in 2019. The H -band data were reduced using DoPhot (Schechter et al., 1993).

We note that in the approximations that the magnified data uniformly sample the magnification range $A_{\text{low}} \leq A \leq A_{\text{high}}$ with n points and that the photometric errors are constant in flux (generally appropriate if all the observations are below sky), the addition of m points at baseline $A_{\text{base}} = 1$ will improve the precision of color measurement by a factor,

$$\frac{\sigma_{\text{w/o-base}}}{\sigma_{\text{with-base}}} = \sqrt{1 + K \frac{m}{m+n}}; \quad K \equiv 12 \frac{n-1}{n+1} \left(\frac{\delta A}{\Delta A} \right)^2, \quad (3)$$

where $\delta A \equiv [(A_{\text{high}} + A_{\text{low}})/2 - A_{\text{base}}]$ and $\Delta A \equiv (A_{\text{high}} - A_{\text{low}})$. Equation (3) can be derived by explicit evaluation of the more general formula $\sigma(\text{slope}) = \sigma_{\text{meas}}/\sqrt{n \text{var}(A)}$ (Gould, 2003). Of course, the conditions underlying Equation (3) will never apply exactly, but it can give a good indication of the utility of baseline observations. In our case $K = 12(4/6)(21.5/21)^2 = 8.4$,

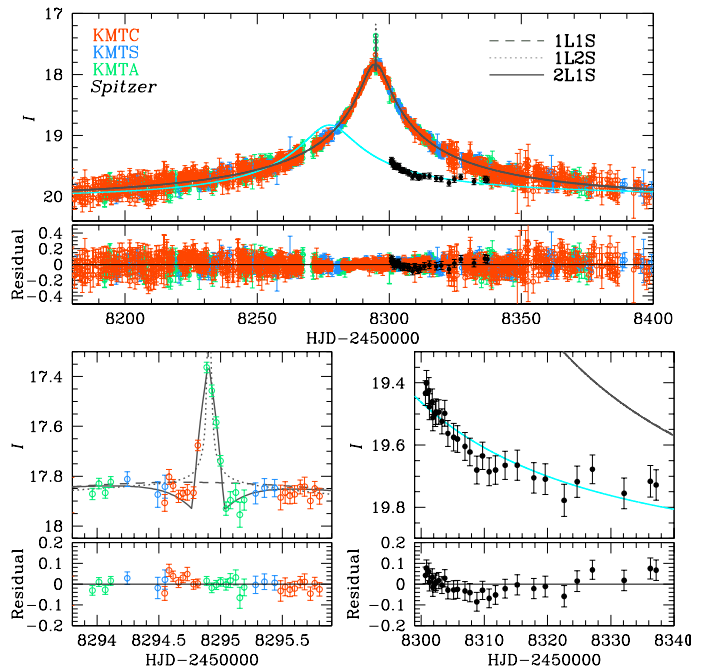


Figure 1. Light curve and best fit model for KMT-2018-BLG-0029. The cusp crossing of the anomaly (lower-left panel) is covered by five points, but the approaches to and from this crossing trace the overall “dip” that typically characterizes transverse cusp approaches. These features are caused by a planet with mass ratio $q = 1.8 \pm 0.2 \times 10^{-5}$, the lowest of any microlensing planet to date by more than a factor two. The *Spitzer* “ L -band” data, which are shown in greater detail in the lower-right panel, have been aligned (as usual) to the I -band scale by $f_{\text{display}} = (f_L - f_{b,L})(f_{s,I}/f_{s,L}) + f_{b,I}$ (and then converted to magnitudes). Their role in measuring the microlens parallax π_E is greatly aided by the IHL color-color relation which constrains the ratio in this expression $(f_{s,I}/f_{s,L}) = 10^{-0.4(I-L)}$ to a few percent. See Section 4.3. The combined *Spitzer* and ground data jointly imply a host mass of $M \sim 1.06 M_{\odot}$ and a distance of $D_L \sim 2.73$ kpc. See Section 6. Paczyński (1L1S, dashed line) and binary-source (1L2S, dotted line) models are clearly excluded by the data.

so the predicted improvement was a factor 2.4. The actual improvement was a factor 2.0, mainly due to worse conditions (hence larger errors) at baseline.

3. GROUND-BASED LIGHT CURVE ANALYSIS

3.1. Static Models

With the exception of five “high points” near the peak of the event, the KMT light curve (Figure 1) looks essentially like a standard single-lens single-source (1L1S) Paczyński (1986) event, which is characterized by three geometric parameters (t_0, u_0, t_E), i.e., the time of lens-source closest approach, the impact parameter of this approach (normalized to θ_E), and the Einstein timescale, $t_E = \theta_E/\mu_{\text{rel}}$. The five high points span just 4.4 hours, and they are flanked by points taken about one hour before and after this interval that are qualitatively consistent with the underlying 1L1S curve. However, the neighboring few hours of data on each side

of the spike actually reveal a gentle “dip” within which the spike erupts. Hence, the pronounced perturbation is very short, i.e., of order a typical source diameter crossing time $2t_* \equiv 2\theta_*/\mu_{\text{rel}}$, where θ_* is the angular radius of the source. Given that the perturbation takes place at peak, the most likely explanation is that the lens has a companion, for which the binary-lens axis is oriented very nearly at $\alpha = \pm 90^\circ$ relative to μ_{rel} . Moreover, the source must be passing over either a cusp or a narrow magnification ridge that extends from a cusp.

Notwithstanding this naive line of reasoning, we conduct a systematic search for binary-lens solutions. We first conduct a grid search over an (s, q) grid, where s is the binary separation in units of θ_E and q is the binary mass ratio. We fit each grid point with a seven-parameter (“standard”) model $(t_0, u_0, t_E, s, q, \alpha, \rho)$, where (s, q) are held fixed and the five other parameters are allowed to vary. The three Paczyński parameters are seeded at their 1L1S values, while α is seeded at six different values drawn uniformly from the unit circle. The last parameter, $\rho \equiv \theta_*/\theta_E = t_*/t_E$ is seeded at $\rho = (4.4 \text{ hr})/2t_E \rightarrow 1 \times 10^{-3}$ following the argument given above. In addition to these non-linear parameters there are two linear parameters for each observatory, i.e., the source flux f_s and the blended flux f_b . Hence, the observed flux is modeled as $F(t) = f_s A(t) + f_b$, where $A(t)$ is the time-dependent magnification at a given observatory.

This grid search yields only one local minimum, which we refine by allowing all seven parameters to vary during the χ^2 minimization. See Figure 1 and Table 1. As anticipated, the binary axis is perpendicular to μ_{rel} . See Figure 2 for the caustic geometry.

3.2. Binary Source Model

In principle, the short-lived “bumps” induced on the light curve by planets (such as the one in Figure 1) can be mimicked by configurations in which there are two sources (1L2S) instead of two lenses (2L1S) (Gaudi, 1998). Hence, unless there are obvious caustic features, one should always check for 1L2S solutions. In the present case, while there are caustic features, they are less than “completely obvious”.

Relative to 1L1S (Paczynski, 1986) models, the 1L2S model has four additional parameters: the $(t_0, u_0)_2$ peak parameters of the second source, ρ_2 , i.e., the radius ratio of the second source to θ_E , and $q_{F,I}$, the I -band flux ratio of the second source to the first.

Figure 1 shows the best-fit 1L2S model, and Table 2 shows the best-fit parameters. For completeness, this table also shows the best fit 1L1S model. The 1L2S model has $\Delta\chi^2 = 130$ relative to the standard 2L1S model. Moreover, it does not qualitatively match the features of the light curve, as shown in Figure 1. Therefore, we exclude 1L2S models.

3.3. Ground-Based Parallax

Because the event is quite long, $t_E > 100$ day, the ground-based light curve alone is likely to put significant

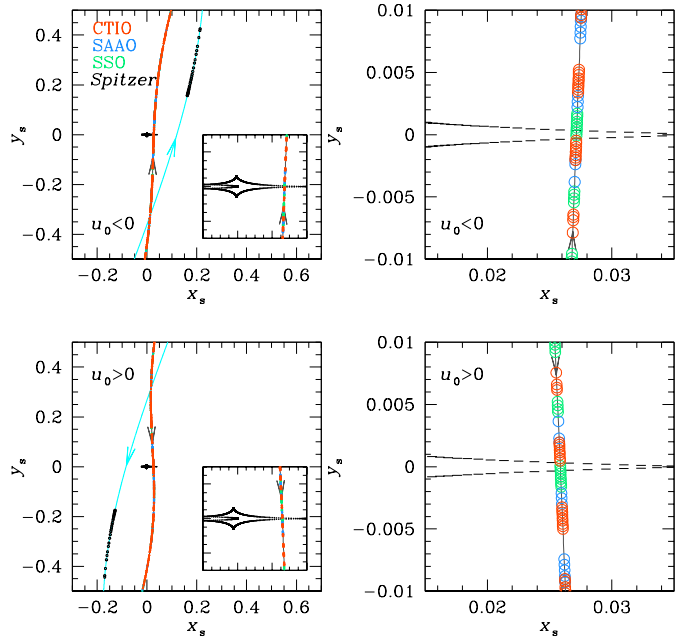


Figure 2. Caustic geometries for the two parallax solutions ($u_0 > 0$ and $u_0 < 0$). The insets show the times of the ground-based observations, color-coded by observatory, with the source size shown to scale. The right panels are zooms of these insets.

constraints on the microlens parallax π_E . It is important to evaluate these constraints in order to compare them with those obtained from the *Spitzer* light curve, as a check against possible systematics in either data set. We therefore begin by fitting for parallax from the ground-based light curve alone, introducing two additional parameters ($\pi_{E,N}, \pi_{E,E}$), i.e., the components of π_E in equatorial coordinates.

We also introduce two parameters for linearized orbital motion $\gamma \equiv ((ds/dt)/s, d\alpha/dt)$ because these can be correlated with π_E (Batista et al., 2011; Skowron et al., 2011). Here ds/dt is the instantaneous rate of change of s , and $d\alpha/dt$ is the instantaneous rate of change of α , both evaluated at t_0 . We expect (and then confirm) that γ may be relatively poorly constrained and so range to unphysical values. We therefore limit the search to $\beta < 0.8$, where β is the ratio of projected kinetic to potential energy (Dong et al., 2009),

$$\beta \equiv \left| \frac{KE_{\perp}}{PE_{\perp}} \right| = \frac{\kappa(y\Gamma)^2 \pi_E}{8\pi^2 \theta_E} \gamma^2 \left(\frac{s}{\pi_E + \pi_s/\theta_E} \right)^3, \quad (4)$$

and where we adopt $\theta_* = 0.70 \mu\text{as}$ from Section 4.2 (and thus, $\theta_E = \theta_*/\rho$) and $\pi_s = 0.12$ for the source parallax. We note that while bound orbits strictly obey $\beta < 1$, we set the limit slightly lower because of the extreme paucity of highly eccentric planets, and the very low probability of observing them at a phase and orientation such that $\beta > 0.8$. We find that with β (and thus γ) so restricted, γ is neither significantly constrained nor strongly correlated with π_E . Hence, we eliminate it from

Table 1
BEST-FIT SOLUTIONS FOR GROUND-ONLY DATA

Parameters	Standard	Parallax models	
		$u_0 > 0$	$u_0 < 0$
χ^2/dof	1855.231/1852	1849.908/1850	1849.504/1850
t_0 (HJD')	8294.702 ± 0.023	8294.709 ± 0.025	8294.704 ± 0.027
u_0	0.028 ± 0.003	0.026 ± 0.002	-0.027 ± 0.002
t_E (days)	169.106 ± 20.595	176.815 ± 13.742	172.151 ± 14.743
s	1.000 ± 0.002	0.999 ± 0.003	1.000 ± 0.002
q (10^{-5})	1.870 ± 0.243	1.817 ± 0.267	1.816 ± 0.215
α (rad)	1.529 ± 0.005	1.529 ± 0.005	-1.529 ± 0.006
ρ (10^{-4})	4.603 ± 0.772	4.414 ± 0.683	4.577 ± 0.693
$\pi_{E,N}$	-	-0.111 ± 0.084	-0.266 ± 0.149
$\pi_{E,E}$	-	0.103 ± 0.045	0.089 ± 0.035
π_E	-	0.151 ± 0.080	0.280 ± 0.126
ϕ_π	-	2.391 ± 0.570	2.819 ± 0.673
f_S (CTIO)	0.029 ± 0.003	0.028 ± 0.003	0.029 ± 0.003
f_B (CTIO)	0.123 ± 0.001	0.129 ± 0.003	0.129 ± 0.003
t_* (days)	0.078 ± 0.009	0.078 ± 0.009	0.079 ± 0.009

Notes, $\pi_E \equiv \sqrt{\pi_{E,N}^2 + \pi_{E,E}^2}$, $\phi_\pi \equiv \tan^{-1}(\pi_{E,E}/\pi_{E,N})$, and $t_* \equiv \rho t_E$ are derived quantities and are not fitted independently. All fluxes are on an 18th magnitude scale, e.g., $I_s = 18 - 2.5 \log(f_s)$.

Table 2
BEST-FIT SOLUTIONS FOR 1L1S AND 1L2S MODELS

Parameters	1L1S	1L2S
χ^2/dof	2544.293/1856	1985.237/1852
$t_{0,1}$ (HJD')	8294.715 ± 0.022	8294.639 ± 0.025
$u_{0,1}$	0.026 ± 0.003	0.031 ± 0.003
t_E (days)	179.591 ± 17.963	156.531 ± 12.943
$t_{0,2}$ (HJD')	-	8294.908 ± 0.002
$u_{0,2}$ (10^{-5})	-	1.101 ± 3.348
ρ_2 (10^{-4})	-	1.305 ± 0.785
qF, I (10^{-3})	-	1.851 ± 0.187
f_S	0.028 ± 0.003	0.032 ± 0.003
f_B	0.125 ± 0.001	0.122 ± 0.001

Table 3
DERIVED PHOTOMETRIC PROPERTIES OF SOURCE

Quantity	mag
A_I	3.39
$I_{s,\text{pydia}}$	22.02 ± 0.08
$I_{s,\text{stand}}$	21.84 ± 0.12
H_s	18.24 ± 0.08
$(I_{\text{pydia}} - H)_s$	3.78 ± 0.02
$(I - H)_{0,s}$	0.87 ± 0.03
$(V - I)_{0,s}$	0.78 ± 0.03
$(V - K)_{0,s}$	1.71 ± 0.07

Note, Instrumental I_{pydia} is calibrated to standard I from the tabulated extinction and the known position of the clump. H -band data are on VVV system.

the fit¹.

As usual, we check for a degenerate solution with $u_0 \rightarrow -u_0$ (Smith et al., 2003), which is often called the ‘‘ecliptic degeneracy’’ because it is exact to all orders on the ecliptic (Jiang et al., 2005), and which can be extended to binary and higher-order parameters (Skowron et al., 2011). Indeed, we find a nearly perfect degeneracy. See Table 1.

Before incorporating the *Spitzer* data we must first investigate the color properties of the source.

4. COLOR-MAGNITUDE DIAGRAM (CMD)

The source color and magnitude are important for two reasons. First, they enable a measurement of θ_* , and so of $\theta_E = \theta_*/\rho$ (Yoo et al., 2004). Second, one can combine the source color with a color-color relation to

¹Given that space-based parallax measurements can in principle break the degeneracy between π_E and γ (Han et al., 2016), we again attempt to introduce γ into the combined space-plus-ground fits in Section 5.2. However, we again find that γ is neither significantly constrained nor significantly correlated with π_E . Hence, we suppress γ for the combined fits as well.

derive a constraint on the *Spitzer* source flux (Yee et al., 2015; Calchi Novati et al., 2015). Table 3 lists many photometric properties of the source.

4.1. Source Position on the CMD

The source is heavily extinguished, $A_I \simeq 3.39$. Therefore, the V -band data that are routinely taken by KMT are too noisy to measure a reliable source color. However, as discussed in Section 2, KMT-2018-BLG-0029 (similar to most *Spitzer* targets) was observed at five epochs in H band and then was additionally observed at six epochs near baseline.

We can therefore place the source on an instrumental $(I - H, I)$ CMD by combining these observations with the I -band observations from KMTC, which is located at the same site as the SMARTS telescopes. To do so, we first reduce the KMTC light curve and photometer the stars within a $2' \times 2'$ square on the same instrumental system using pyDIA. We then evaluate the $(I - H)$ instrumental color by regression, finding $(I_{\text{pyDIA}} - H_{\text{ANDICAM}}) = -1.035 \pm 0.019$. In order to apply the method of Yoo et al. (2004) we must com-

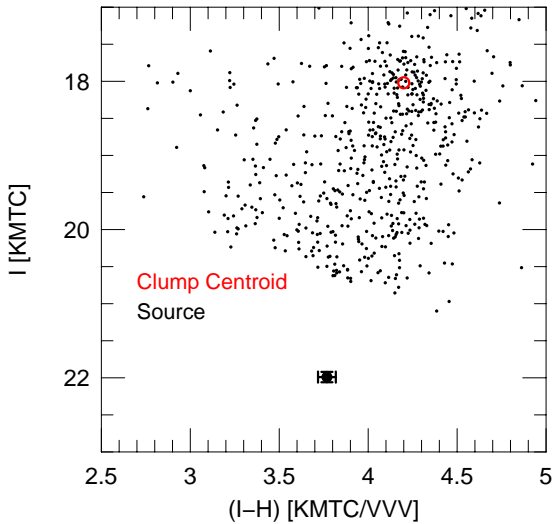


Figure 3. Color-magnitude diagram (CMD) for stars within a $2'$ square centered on KMT-2018-BLG-0029. The I -band data come from pyDIA reductions of KMTC data while the H -band data come from the VVV catalog. The source I magnitude (black) derives from the fit to the light curve while the source $(I - H)$ color comes from regression of the SMARTS ANDICAM H -band light curve (aligned to the VVV system) on the I -band light curve. The red giant clump centroid is shown in red.

pare this color to that of the red giant clump. However, the ANDICAM data do not go deep enough to reliably trace the clump. We therefore align the ANDICAM system to the VVV survey (Minniti et al., 2017), finding $(H_{\text{ANDICAM}} - H_{\text{VVV}}) = 4.817 \pm 0.005$ and therefore $(I_{\text{pyDIA}} - H_{\text{VVV}}) = 3.782 \pm 0.019$. We then find $I_{\text{pyDIA}} = 22.02 \pm 0.02$ by fitting the pyDIA light curve to the best model from Section 3.3. We form an $(I - H, I)$ CMD by cross-matching the KMTC-pyDIA and VVV field stars. Figure 3 shows the source position on this CMD.

4.2. θ_E and μ_{rel}

We next measure the clump centroid on this CMD, finding $[(I - H), I]_{\text{clump}} = (4.20, 18.02) \pm (0.02, 0.04)$, which then yields an offset from the clump of $\Delta[(I - H), I] = (-0.42, 3.98) \pm (0.02, 0.03)$. We adopt $[(V - I), I]_{0, \text{clump}} = (1.06, 14.45)$ from Bensby et al. (2013) and (Nataf et al., 2013), and use the color-color relations of Bessell & Brett (1988), to derive $(V - K, V)_0 = (1.71, 19.21)$. That is, the source is a late G star that is very likely on the turnoff/subgiant branch. Applying the color/surface-brightness relation of Kervella et al. (2004), we find,

$$\theta_* = 0.70 \pm 0.05 \mu\text{as}. \quad (5)$$

Table 4
Spitzer-“ONLY” MODELS

Parameters	$u_0 > 0$	$u_0 < 0$
χ^2/dof	25.293/25	25.475/25
$\pi_{E,N}$	-0.037 ± 0.057	0.042 ± 0.065
$\pi_{E,E}$	0.152 ± 0.019	0.153 ± 0.026
π_E	0.156 ± 0.016	0.159 ± 0.016
ϕ_π	1.810 ± 0.378	1.301 ± 0.430
$f_s(\textit{Spitzer})$	0.565 ± 0.032	0.584 ± 0.032
$f_B(\textit{Spitzer})$	2.519 ± 0.116	2.486 ± 0.123

Note, π_E and ϕ_π are derived quantities and are not fitted independently. All fluxes are on an 18th magnitude scale, e.g., $L_{s, \textit{Spitzer}} = 18 - 2.5 \log(f_{s, \textit{Spitzer}})$.

Combining Equation (5) with ρ and t_E from the ground-based parallax solutions in Table 1, this implies,

$$\theta_E = \frac{\theta_*}{\rho} = 1.56 \pm 0.24 \text{ mas}; \quad \mu_{\text{rel}} = \frac{\theta_E}{t_E} = 3.3 \pm 0.5 \frac{\text{mas}}{\text{yr}}. \quad (6)$$

These values strongly favor a disk lens, $D_L \lesssim 3$ kpc, because otherwise the lens would be massive (thus bright) enough to exceed the observed blended light. However, we defer discussion of the nature of the lens until after incorporating the *Spitzer* parallax measurement into the analysis.

4.3. *IHL* Color-Color Relation

We match field star photometry from KMTC-pyDIA (I) and VVV (H) (Section 4.1) with *Spitzer* (L) photometry within the range $3.6 < (I - H) < 4.5$, to obtain an *IHL* color-color relation

$$I_{\text{pyDIA}} - L = 1.18[(I_{\text{pyDIA}} - H)_s - 3.70] + 3.32 \rightarrow 3.417 \pm 0.022, \quad (7)$$

where the instrumental *Spitzer* fluxes are converted to magnitudes on an 18th mag system. In order to relate Equation (7) to the pySIS magnitudes reported in this paper (e.g., in Tables 1 and 5), we take account of the offset between these two systems (measured very precisely from regression) $I_{\text{pySIS}} - I_{\text{pyDIA}} = -0.120 \pm 0.005$ to obtain

$$I_{\text{pySIS}} - L = 3.297 \pm 0.022, \quad (8)$$

We employ this relation when we incorporate *Spitzer* data in Section 5.

5. PARALLAX ANALYSIS INCLUDING *Spitzer* DATA

5.1. *Spitzer*-“Only” Parallax

As discussed in Section 3.3, it is important to compare the parallax information coming from the ground and *Spitzer* separately before combining them, in order to test for systematics. To trace the information coming from *Spitzer*, we first suppress the parallax information coming from the ground-based light curve by representing it by its seven non-parallax parameters $(t_0, u_0, t_E, s, q, \alpha, \rho)_\oplus$ along with the I -band source flux $f_{s, \oplus}$, as taken from Table 1. For this purpose, we use these eight non-parallax parameters taken from the

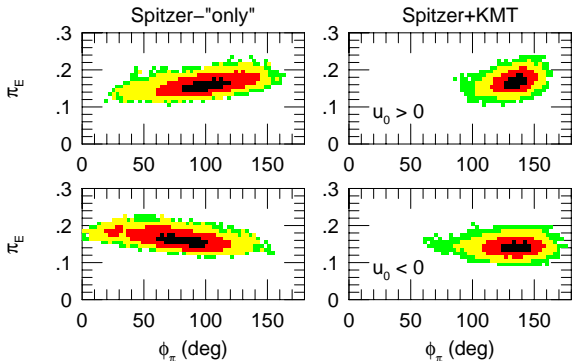


Figure 4. Likelihood contours $-2\Delta \ln L < (1, 4, 9)$ for (black, red, yellow) for the parallax vector π_E in polar coordinates. Green indicates $-2\Delta \ln L > 9$. Although the polar-angle ϕ_π distribution is relatively broad for the *Spitzer*-“only” fits (left panels), the amplitude π_E is nearly constant because the *Spitzer* observations are reasonably close to the Gould & Yee (2012) “cheap parallax” limit. See Section 5.2. When “one-dimensional” parallax information from the ground is added (right panels), the solution is more tightly constrained. See also Figures 5 and 6.

parallax solutions. In this sense, there is some indirect “parallax information” coming from the ground-based fit. However, because we are testing for consistency, we must do this to avoid injecting inconsistent information. (In any case, the standard-model and parallax-model parameters are actually quite similar.) We apply this procedure separately for the two “ecliptic degeneracy” parallax solutions shown in Table 1. In principle, adding *Spitzer* data could generate two separate solutions for each of these, according to whether the lens passes to the left or right of the source as seen from *Spitzer* (Refsdal, 1966; Gould, 1994). In practice, however, these two solutions merge because the *Spitzer* data commence after $t_{0,Spitzer}$ (Gould, 2019).

The left-hand panels of Figure 4 show likelihood contours in polar coordinates for the $u_0 > 0$ and $u_0 < 0$ solutions of the *Spitzer*-“only” analysis. See also Table 4. That is, $\pi_E = |\boldsymbol{\pi}_E|$ is the amplitude and $\phi_\pi = \tan^{-1}(\pi_{E,E}/\pi_{E,N})$ is the polar angle. For both signs of u_0 , the amplitude π_E is nearly constant over a broad range of angles. This can be understood within the context of the argument of Gould & Yee (2012), which was then empirically verified by Shin et al. (2018). In the original argument, a single satellite measurement at the epoch of the ground-based peak, $t_{0,\oplus}$, of a high-magnification event (together with a baseline measurement) would yield an excellent measurement of π_E but essentially zero information about ϕ_π . Because the first *Spitzer* point is six days after $t_{0,\oplus}$, this condition does not strictly hold. However, the mathematical basis of the argument is in essence that $u_{\text{sat}} \gg$

Table 5
BEST-FIT SOLUTIONS FOR GROUND+*Spitzer* DATA

Parameters	Parallax models	
	$u_0 > 0$	$u_0 < 0$
χ^2/dof	1877.366/1877	1881.631/1877
t_0 (HJD')	8294.703 ± 0.026	8294.722 ± 0.025
u_0	0.026 ± 0.002	-0.027 ± 0.003
t_E (days)	179.815 ± 15.247	172.681 ± 16.055
s	0.999 ± 0.002	1.000 ± 0.002
q (10^{-5})	1.811 ± 0.202	1.840 ± 0.214
α (rad)	1.528 ± 0.006	-1.533 ± 0.005
ρ (10^{-4})	4.273 ± 0.643	4.433 ± 0.689
$\pi_{E,N}$	-0.125 ± 0.026	-0.099 ± 0.027
$\pi_{E,E}$	0.114 ± 0.018	0.107 ± 0.023
π_E	0.169 ± 0.017	0.145 ± 0.014
ϕ_π	2.401 ± 0.164	2.317 ± 0.227
f_S (CTIO)	0.027 ± 0.002	0.029 ± 0.003
f_B (CTIO)	0.130 ± 0.001	0.128 ± 0.002
f_S (<i>Spitzer</i>)	0.548 ± 0.058	0.586 ± 0.064
f_B (<i>Spitzer</i>)	2.498 ± 0.064	2.402 ± 0.092
t_* (days)	0.077 ± 0.009	0.077 ± 0.009

Note, π_E , ϕ_π , and t_* are derived quantities and are not fitted independently. All fluxes are on an 18th magnitude scale, e.g., $I_s = 18 - 2.5 \log(f_s)$.

u_\oplus at the time of this “single observation”. This is reasonably well satisfied for the first *Spitzer* observation. At this time $u_\oplus \sim 0.044$. On the other hand, $A(t)_{\text{spitzer}} = 1 + (F(t) - F_{\text{base}})/F_s \rightarrow 5.1$ for the first epoch. Thus², $u_{\text{Spitzer}} \sim 0.199$. If this had truly been a single-epoch measurement, then the parallax contour would have been an “offset circle” (compared to the well-centered circle of Figure 3 of Shin et al. 2018), with extreme parallax values $\pi_{E,\pm} = (\text{AU}/D_\perp)(0.199 \pm 0.044)$, i.e., a factor 1.57 difference. Here $D_\perp \sim 1.3 \text{ AU}$ is the projected Earth-*Spitzer* separation at the measurement epoch. However, the rest of the *Spitzer* light curve then restricts this circle to an arc. See Figures 1 and 2 of Gould (2019), which also illustrate how the two *Spitzer*-“only” solutions (for a given sign of $u_0 \equiv u_{0,\oplus}$) merge. Figure 5 shows the π_E contours in Cartesian coordinates for the six cases. Here we focus attention on four of these cases, (ground-only, *Spitzer*-“only”) $\times (u_0 < 0, u_0 > 0)$.

These show that the ground-only and *Spitzer*-“only” parallax contours are quite consistent for the $u > 0$ case and marginally inconsistent for the $u < 0$ case. The levels of consistency can be more precisely gauged from Figure 6, which shows overlapping contours. Because one of these two cases is consistent, there is no evidence for systematics in either data set. That is, only one of the two cases can be physically correct, so only if both were inconsistent would the comparison provide evidence of systematics.

5.2. Full Parallax Models

We therefore proceed to analyze the ground- and space-based data together. The resulting microlens parameters for the two cases ($u_{0,\oplus} < 0$ and $u_{0,\oplus} > 0$) are shown in Table 5. The parallax contours are shown in

²For point lenses, $u = [2((1 - A^{-2})^{-1/2} - 1)]^{1/2}$.

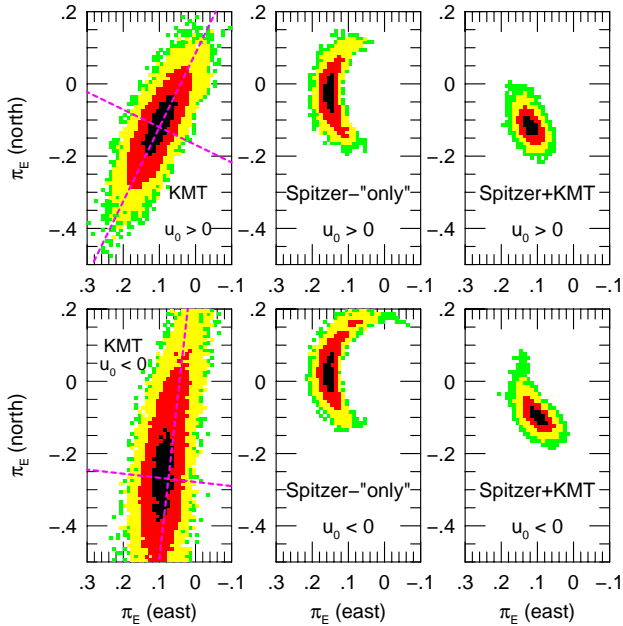


Figure 5. 6-panel diagram of $(\pi_{E,N}, \pi_{E,E})$ Cartesian contours. The upper panels show the $u_0 > 0$ solutions, while the lower panels show the $u_0 < 0$ solutions. From left to right, we display ground-only, *Spitzer*-“only”, and combined parallaxes. Black, red, and yellow indicate relative likelihoods $-2\Delta \ln L < 1, 4, 9$ respectively. Green represents $-2\Delta \ln L > 9$. The ground-only data yield approximately linear, “one-dimensional” constraints (Gould et al., 1994; Smith et al., 2003). The *Spitzer*-“only” data yield an arc opening to the west (direction of *Spitzer*) because they begin post-peak and are falling rapidly (Gould, 2019). However, the arc is confined to an arcllet of relatively constant π_E amplitude (see Figure 4) because the *Spitzer* observations begin when the ground data are still highly magnified. For at least one case ($u > 0$) the left and center panels are quite consistent, implying that there is no evidence for systematics. Hence, the two data sets can be combined to yield significantly smaller error bars (right). The magenta lines in the left panels show the principal axes defined by the 2σ contour. For $u_0 > 0$, the contours are nearly elliptical and the minor axis $\psi_{\text{short}} = -116^\circ$ is almost perfectly aligned to the direction of the Sun at peak: -117° , both of which reflect “ideal” 1-D parallaxes. For $u_0 < 0$, the ellipse deviates from both conditions. See text.

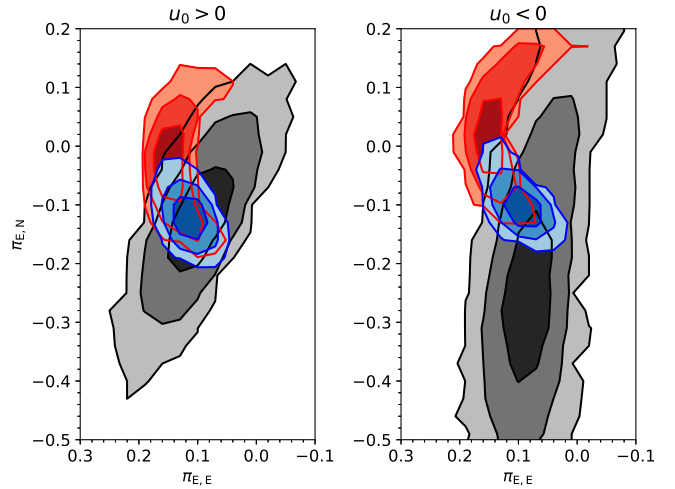


Figure 6. Overlap of three sets of contours shown in Figure 5 for each of the two parallax solutions. This makes it easier to see that for $u_0 > 0$ the ground-only and *Spitzer*-“only” solutions are quite consistent, showing that there is no evidence for systematics. Then, the fact that these solutions show some tension for $u_0 < 0$ implies that this solution is somewhat disfavored.

the right-hand panels of Figures 4 and 5 and also superposed on the ground-only and *Spitzer*-“only” contours in Figure 6.

The first point to note is that while the χ^2 values of the two $\pm u_{0,\oplus}$ topologies are nearly identical for the ground-only and *Spitzer*-“only” solutions, the combined solution favors $u_0 > 0$ by $\Delta\chi^2 = 4.3$. This reflects the marginal inconsistency for the $u_0 < 0$ case that we identified in Section 5.1. See Figure 6.

The next point is that the effect of the ground-based parallax ellipse (left panels of Figure 5) is essentially to preferentially select a subset of the *Spitzer*-“only” arc (middle panels). This is especially true of the $u_0 > 0$ solution, which we focus on first. The long axis of the ground-only ellipse (evaluated by the $\Delta\chi^2 = 4$ contour) is aligned at an angle $\psi_{\text{long}} \simeq -26^\circ$ north through east, implying that the short axis is oriented at $\psi_{\text{short}} \simeq -116^\circ$. This is close to the projected position of the Sun at $t_{0,\oplus}$, $\psi_\odot = -117^\circ$, which means that the main ground-based parallax information is coming from Earth’s instantaneous acceleration near the peak of the event. This is somewhat surprising because this instantaneous acceleration is rather weak ($\sim 17\%$ of its maximum value) due to the fact that the event is nearly at opposition. However, it confirms that despite the large value of $t_E \sim 175$ days, it is primarily the highly magnified region near the peak, where the fractional photometry errors are smaller, that contributes substantial parallax information. The measurement of the component

Table 6

PHYSICAL PARAMETERS FOR GROUND+SPITZER MODELS

Quantity	$u_0 > 0$	$u_0 < 0$
$M_{\text{host}} [M_{\odot}]$	$1.06^{+0.20}_{-0.17}$	$1.24^{+0.24}_{-0.20}$
$M_{\text{planet}} [M_{\oplus}]$	$6.41^{+0.89}_{-0.75}$	$7.61^{+1.05}_{-0.89}$
a_{\perp} [au]	$3.94^{+0.35}_{-0.31}$	$4.38^{+0.40}_{-0.36}$
D_L [kpc]	$2.73^{+0.26}_{-0.22}$	$3.07^{+0.27}_{-0.24}$
$\mu_{\text{hel},N}$ [mas/yr]	$-2.12^{+0.44}_{-0.43}$	$-2.10^{+0.57}_{-0.52}$
$\mu_{\text{hel},E}$ [mas/yr]	$3.57^{+0.53}_{-0.49}$	$3.33^{+0.67}_{-0.57}$
$v_{L,LSR,l}$ [km/s]	-60^{+45}_{-45}	-71^{+51}_{-51}
$v_{L,LSR,b}$ [km/s]	-47^{+35}_{-35}	-50^{+39}_{-39}

of parallax along this ψ_{short} direction ($\pi_{E,\parallel}$) not only has smaller statistical errors than $\pi_{E,\perp}$ (as illustrated by the ellipse), but is also less subject to systematic errors because it is much less dependent on long term photometric stability over the season. From inspection of the left panel of Figure 6, it is clear that the intersection of the ground-only and *Spitzer*-“only” contours is unique and would remain essentially the same even if the ground-only contours were displaced along the long axis.

The situation is less satisfying for the $u_{0,\oplus} < 0$ solution in several respects. These must be evaluated within the context that, overall, this solution is somewhat disfavored by the marginal inconsistency between the ground-only and *Spitzer*-“only” solutions discussed in Section 5.1. First, the error ellipse is oriented at $\psi_{\text{short}} \simeq -97^\circ$, which is 20° away from the projected position of the Sun at $t_{0,\oplus}$. This implies that the dominant parallax information is coming from after peak rather than symmetrically around peak, which already indicates that it is less robust and more subject to long-timescale systematics. Related to this, the uncertainties in the ψ_{long} direction are larger. Hence, we should consider how the solution would change for the case that systematics have shifted the ground-only error ellipse along the long axis by a few sigma. From inspection of the right panel of Figure 6, this would tend to create a second, rather weak, minimum near $(\pi_{E,N}, \pi_{E,E}) \simeq (+0.16, +0.04)$. However, even under this hypothesis, this new minimum would suffer even stronger inconsistency between ground-only and *Spitzer*-“only” solutions than the current minimum.

We conclude that the $u_0 < 0$ solution is disfavored, and even if it is nevertheless correct, its parallax is most likely given by the displayed minimum rather than a secondary minimum that would be created if the ground-based contours were pushed a few sigma to the north. Moreover, the parallax amplitude $\pi_E = |\pi_E|$ is actually similar for the two minima (see lower panels of Figure 4), and it is only π_E that enters the mass and distance determinations. We conclude that the physical parameter estimates, which we give in Section 6, are robust against the typical systematic errors that are described above.

6. PHYSICAL PARAMETERS

We evaluate the physical parameters of the system by directly calculating their values for each element of the Monte Carlo Markov chain (MCMC). In particular, for each element, we evaluate $\theta_* = \theta_{*,0}(1 + \epsilon_*)$, where $\theta_{*,0} = 0.70 \mu\text{as}(f_{s,\text{pySIS}}/0.028)^{1/2}$ and $\epsilon_* = 4\%$ is treated as a random variation. However, we note that the largest source of uncertainty in the physical parameters is the $\sim 15\%$ error in ρ . These physical parameters are reported in Table 6. For our analysis, we adopt a source distance $D_S = R_0 = 8.2\text{kpc}$, and source motions in the heliocentric frame drawn from a distribution derived from *Gaia* data³, $\boldsymbol{\mu}_s(l, b) = (-5.7, 0.0)\text{mas yr}^{-1}$, $\sigma(\boldsymbol{\mu}_s) = (3.4, 2.7)\text{mas yr}^{-1}$.

We note that while the central values for the lens velocity in the frame of the local standard of rest (LSR) are large, they are consistent within their 1σ errors with typical values for disk objects. These large errors are completely dominated by the uncertainty in the source proper motion, which propagates to errors in $\mathbf{v}_{L,LSR}$ of $D_L\sigma(\boldsymbol{\mu}_s) \sim (44, 35)\text{km s}^{-1}$ for, e.g., the $u_0 > 0$ solution. These are then added in quadrature to the much smaller terms from other sources of error.

We next test whether the lens mass and distance estimates shown in Table 6 are consistent with limits on lens light in baseline images. For this purpose, we take r and i images using the 3.6m Canada-France-Hawaii Telescope (CFHT) at Mauna Kea, Hawaii, which are both deeper and at higher resolution than the KMT image. We align the two systems photometrically and find $I_{\text{base,pyDIA}} = 20.085 \pm 0.044$, which implies blended flux (in these higher resolution images) of $I_{b,\text{pyDIA}} = 20.29 \pm 0.07$. We then compare the position of the clump $I_{cl,\text{pyDIA}} = 18.02$ to that expected from standard photometry (Nataf et al., 2013) and the estimated extinction $A_I = 3.39$, i.e., $I_{cl,\text{stand}} = 17.84$ to derive a calibration offset $\Delta I = -0.18 \pm 0.09$. This yields $I_{b,\text{stand}} = 20.11 \pm 0.12$.

In asking whether the upper limits on lens flux implied by this blended light are consistent with the physical values in Table 6, we should be somewhat conservative and assume that the lens lies behind the full column of dust seen toward the bulge, $A_{I,l} = 3.39$. Then, $I_{0,b} = 16.72 \pm 0.12$, and hence (incorporating the 1σ range of distances for $u_0 > 0$), the corresponding absolute magnitude range is $M_{I,l} = 4.54 \pm 0.22$. This range is quite consistent with expectations for the $M_{\text{host}} = 1.06^{+0.20}_{-0.17}$ host reported for the $u_0 > 0$ solution.

We conclude that the blended light is a good candidate for the light expected from the lens. However, given the faintness of the source and the difficulties of seeing-limited observations (even with very good seeing), we refrain from concluding that we have in fact

³Because the actual line of sight $(l, b) = (-0.09, +1.95)$ is heavily extinguished, we evaluate the *Gaia* proper-motion ellipse at the symmetric position $(l, b) = (-0.09, -1.95)$. We consider stars within a $2'$ square of this position and restrict attention to Bulge giants defined by $G < 18$ and $B_p - R_p > 2.25$. We eliminate four outliers and make our evaluation based on the remaining 226 stars, the majority of which are clump giants.

detected the lens, and so we do not further modify our physical-parameter estimates based on these baseline-light measurements.

Nevertheless, we note that, the corresponding calculation for the $u_0 < 0$ solution leads to mild ($\sim 1\sigma$) tension, rather than simple consistency. When combined with the earlier indications of marginal inconsistency, we consider that overall the $u_0 < 0$ solution is disfavored. We therefore report our final results as those of the $u_0 > 0$ solution.

7. DISCUSSION

KMT-2018-BLG-0029Lb has the lowest planet-host mass ratio $q = 0.18 \times 10^{-4}$ of any microlensing planet to date. Although eight planets had previously been discovered in the range of $0.5\text{--}1.0 \times 10^{-4}$, including seven analyzed by Udalski et al. (2018) and one discovered subsequently (Ryu et al., 2019b), none came even within a factor of two of the planet that we report here. This discovery therefore proves that the previously discovered pile-up of planets with Neptune-like planet-host mass ratios does not result from a hard cut-off in the underlying distribution of planets. However, it will require more than a single detection to accurately probe the frequency of planets in this sub-Neptune mass-ratio regime. It is somewhat sobering that after 16 years of microlensing planet detections there are only nine with well measured mass ratios⁴ $q \leq 1 \times 10^{-4}$. Hence, it is worthwhile to ask about the prospects for detecting more.

7.1. Prospects for Very Low q Microlensing Planets

Of the nine such events, five were found 2005–2013 and four were found 2016–2018. These two groups have strikingly different characteristics. Four (OGLE-2005-BLG-390, OGLE-2007-BLG-368, MOA-2009-BLG-266, and OGLE-2013-BLG-0341) from the first group revealed their planets via planetary caustics, and only one (OGLE-2005-BLG-169) via central or resonant caustics. By contrast, all four from the second group revealed their planets via central or resonant caustics and all with impact parameters $u_0 \lesssim 0.05$. Another telling difference is that follow-up observations played a crucial or very important role in characterizing the planet for four of the five in the first group⁵, while follow-up observations did not play a significant role in characterizing any of the four planets in the second group. Finally, the overall rate of discovery approximately doubled from the first to the second period.

The second period, 2016–2018, coincides with the full operation of KMTNet in its wide-field, 24/7 mode

⁴Note that while OGLE-2017-BLG-0173L (Hwang et al., 2018) definitely has a mass ratio $q < 1 \times 10^{-4}$, it is not included in this sample because it has two degenerate solutions with substantially different q , and hence its mass ratio cannot be regarded as “well measured”.

⁵For the fifth, OGLE-2013-BLG-0341L (Gould et al., 2014), there were also very extensive follow-up observations, which were important for characterizing the binary-star system containing the host, but these did not play a major role in the characterization of the planet itself.

(Kim et al., 2018b,c). The original motivation for KMTNet was to find and characterize low-mass planets without requiring follow-up observations (Kim et al., 2018a). All four planets from the second group were intensively observed by KMTNet, with the previous three all in high-cadence ($\Gamma = 4 \text{ hr}^{-1}$) fields and KMT-2018-BLG-0029Lb in a $\Gamma = 1 \text{ hr}^{-1}$ field. It should be noted that OGLE-2016-BLG-1195Lb was discovered and independently characterized (i.e., without any KMTNet data) by OGLE and MOA (Bond et al., 2017). In this sense, it is similar to the OGLE-2013-BLG-0341LBb, which would have been discovered and characterized by OGLE and MOA data, even without follow-up data.

The above summary generally confirms the suggestion of Udalski et al. (2018) that the rate of low-mass planet discovery has in fact doubled in the era of continuous wide-field surveys. However, it also suggests that this discovery mode (i.e., without substantial follow-up observations) is “missing” many low-mass planets that were being discovered in the previous period. Apart from OGLE-2013-BLG-0341, which would have been characterized without follow-up, three of the other four low-mass planets from that period were all discovered in what would today be considered “outlying fields”, with Galactic coordinates (l, b) of OGLE-2005-BLG-169 (0.67, -4.74), OGLE-2007-BLG-368 ($-1.65, -3.69$), MOA-2009-BLG-266 ($-4.93, -3.58$). These regions are currently observed by KMTNet at $\Gamma = (1, 1, 0.4) \text{ hr}^{-1}$. Only OGLE-2005-BLG-390 (2.34, -2.92) lies in what is now a high-cadence KMT field.

Moreover, the rate of discovery of microlensing events in these outlying fields is much higher today than it was when these four planets were discovered. Hence, while there is no question that the pure-survey mode has proved more efficient at finding low-mass planets, the rate of discovery could be enhanced by aggressive follow-up observations. See also Figure 8 from Ryu et al. (2019a).

7.2. Additional *Spitzer* Planet

KMT-2018-BLG-0029Lb is the sixth published planet in the *Spitzer* statistical sample that is being accumulated to study the Galactic distribution of the planets (Yee et al., 2015; Calchi Novati et al., 2015). The previous five were⁶ OGLE-2014-BLG-0124Lb (Udalski et al., 2015a), OGLE-2015-BLG-0966Lb (Street et al., 2016), OGLE-2016-BLG-1190Lb (Ryu et al., 2017b), OGLE-2016-BLG-1195Lb (Bond et al., 2017; Shvartzvald et al., 2017), and OGLE-2017-BLG-1140Lb (Calchi Novati et al., 2018).

While it is premature to derive statistical implications from this sample, it is important to note that the planetary signature in the KMT-2018-BLG-0029 light curve remained hidden in the real-time photometry, although the pipeline re-reductions did yield strong hints of a planet. Nevertheless, TLC re-reductions were required

⁶In addition, there were two other *Spitzer* parallaxes for planets that are not in the statistical sample, OGLE-2016-BLG-1067Lb (Calchi Novati et al., 2019) and OGLE-2018-BLG-0596Lb (Jung et al., 2019b).

for a confident signal. Hence, the history of this event provides strong caution that careful review of all *Spitzer* microlensing events, with TLC re-reductions in all cases with possible hints of planets, will be crucial for fully extracting information about the Galactic distribution of planets from this sample.

ACKNOWLEDGMENTS

Work by AG was supported by AST-1516842 from the US NSF and by JPL grant 1500811. AG received support from the European Research Council under the European Unions Seventh Framework Programme (FP 7) ERC Grant Agreement n. [321035]. Work by C.H. was supported by the grant (2017R1A4A1015178) of the National Research Foundation of Korea. This research has made use of the KMTNet system operated by the Korea Astronomy and Space Science Institute (KASI) and the data were obtained at three host sites of CTIO in Chile, SAAO in South Africa, and SSO in Australia. We are very grateful to the instrumentation and operations teams at CFHT who fixed several failures of MegaCam in the shortest time possible, allowing its return onto the telescope and these crucial observations. W.Z. and S.M. acknowledges support by the National Science Foundation of China (Grant No. 11821303 and 11761131004). MTP was supported by NASA grants NNX14AF63G and NNG16PJ32C, as well as the Thomas Jefferson Chair for Discovery and Space Exploration. This research uses data obtained through the Telescope Access Program (TAP), which has been funded by the National Astronomical Observatories of China, the Chinese Academy of Sciences, and the Special Fund for Astronomy from the Ministry of Finance.

REFERENCES

- Alard, C. & Lupton, R.H., 1998, A Method for Optimal Image Subtraction, *ApJ*, 503, 325
- Albrow, M. D., Horne, K., Bramich, D. M., et al. 2009, Difference imaging photometry of blended gravitational microlensing events with a numerical kernel, *MNRAS*, 397, 2099
- Batista, V., Gould, A., Dieters, S. et al. 2011, MOA-2009-BLG-387Lb: a massive planet orbiting an M dwarf, *A&A*, 529, 102
- Batista, V., Beaulieu, J.-P., Gould, A., et al. 2014, MOA-2011-BLG-293Lb: First Microlensing Planet Possibly in the Habitable Zone, *ApJ*, 780, 54
- Batista, V., Beaulieu, J.-P., Bennett, D.P., et al. 2015, Confirmation of the OGLE-2005-BLG-169 Planet Signature and Its Characteristics with Lens-Source Proper Motion Detection, *ApJ*, 808, 170
- Bennett, D.P., Anderson, J., Bond, I.A., et al. 2006, Identification of the OGLE-2003-BLG-235/MOA-2003-BLG-53 Planetary Host Star, *ApJ*, 647, L171
- Bennett, D.P., Rhie, S.H., Nikolaev, S. et al. 2010, Masses and Orbital Constraints for the OGLE-2006-BLG-109Lb,c Jupiter/Saturn Analog Planetary System, *ApJ*, 713, 837
- Bennett, D.P., Bhattacharya, A., Anderson, J., et al. 2015, Confirmation of the Planetary Microlensing Signal and Star and Planet Mass Determinations for Event OGLE-2005-BLG-169, *ApJ*, 808, 169
- Bensby, T. Yee, J.C., Feltzing, S. et al. 2013, Chemical evolution of the Galactic bulge as traced by microlensed dwarf and subgiant stars. V. Evidence for a wide age distribution and a complex MDF, *A&A*, 549A, 147
- Bessell, M.S., & Brett, J.M. 1988, JHKLM photometry - Standard systems, passbands, and intrinsic colors, *PASP*, 100, 1134
- Bond, I.A., Udalski, A., Jaroszyński, M. et al. 2004, OGLE 2003-BLG-235/MOA 2003-BLG-53: A Planetary Microlensing Event, *ApJ*, 606, L155
- Bond, I.A., Bennett, D.P., Sumi, T. et al. 2017, The lowest mass ratio planetary microlens: OGLE 2016-BLG-1195Lb, *MNRAS*, 469, 2434
- Calchi Novati, S., Gould, A., Yee, J.C., et al. 2015, *Spitzer* IRAC Photometry for Time Series in Crowded Fields, *ApJ*, 814, 92
- Calchi Novati, S., Suzuki, D., Udalski, A., et al. 2019, Microlensing Parallax for OGLE-2016-BLG-1067: a sub-Jupiter Orbiting an M-dwarf in the Disk, 157, 121
- Calchi Novati, S., Skowron, J., Jung, Y.K., et al. 2018, *Spitzer* Opens New Path to Break Classic Degeneracy for Jupiter-mass Microlensing Planet OGLE-2017-BLG-1140Lb, 155, 261
- DePoy, D.L., Atwood, B., Belville, S.R., et al. 2003, A Novel Double Imaging Camera (ANDICAM), *SPIE* 4841, 827
- Dong, S., Udalski, A., Gould, A., et al. 2007, First Space-Based Microlens Parallax Measurement: *Spitzer* Observations of OGLE-2005-SMC-001, *ApJ*, 664, 862
- Dong, S., Gould, A., Udalski, A., et al. 2009, OGLE-2005-BLG-071Lb, the Most Massive M Dwarf Planetary Companion?, *ApJ*, 695, 970
- Gaudi, B.S. 1998, Distinguishing Between Binary-Source and Planetary Microlensing Perturbations, *ApJ*, 506, 533
- Gaudi, B.S., Bennett, D.P., Udalski, A. et al. 2008, Discovery of a Jupiter/Saturn Analog with Gravitational Microlensing, *Science*, 319, 927
- Gould, A. 1992, Extending the MACHO search to about 10^6 solar masses, *ApJ*, 392, 442
- Gould, A. 1994, MACHO parallaxes from a single satellite, *ApJL*, 421, L75
- Gould, A. 2000, A Natural Formalism for Microlensing, *ApJ*, 542, 785
- Gould, A. 2003, χ^2 and Linear Fits, 2003astro.ph.10577
- Gould, A. 2019, Osculating Versus Intersecting Circles in Space-Based Microlens Parallax Degeneracies, *JKAS*, submitted, arXiv:1905.06770
- Gould, A. & Yee, J.C. 2012, Cheap Space-based Microlens Parallaxes for High-magnification Events, *ApJ*, 755, L17
- Gould, A., Udalski, A., Shin, I.-G. et al. 2014, A terrestrial planet in a ~ 1 -AU orbit around one member of a ~ 15 -AU binary, *Science*, 345, 46

- Gould, A., Carey, S., & Yee, J. 2013, Spitzer Microlens Planets and Parallaxes, 2013spitz.prop.10036
- Gould, A., Carey, S., & Yee, J. 2014, Galactic Distribution of Planets from Spitzer Microlens Parallaxes, 2014spitz.prop.11006
- Gould, A., Yee, J., & Carey, S., 2015a, Galactic Distribution of Planets From High-Magnification Microlensing Events, 2015spitz.prop.12013
- Gould, A., Yee, J., & Carey, S., 2015b, Degeneracy Breaking for K2 Microlens Parallaxes, 2015spitz.prop.12015
- Gould, A., Yee, J., & Carey, S., 2016, Galactic Distribution of Planets Spitzer Microlens Parallaxes, 2015spitz.prop.13005
- Gould, A., Miralda-Escudé, J. & Bahcall, J.N. 1994, Microlensing Events: Thin Disk, Thick Disk, or Halo?, ApJ, 423, L105
- Han, C., Udalski, A., Lee, C.-U., et al. 2016, ApJ, 827, 11
- Hwang, K.-H., Udalski, A., Shvartzvald, Y. et al. 2018, OGLE-2017-BLG-0173Lb: Low Mass-Ratio Planet in a “Hollywood” Microlensing Event, AJ, 155, 20
- Jiang, G., DePoy, D.L., Gal-Yam, A., et al. 2005, OGLE-2003-BLG-238: Microlensing Mass Estimate of an Isolated Star, ApJ, 617, 1307
- Jung, Y. K., Gould, A., & Zang, W., et al. 2019, KMT-2017-BLG-0165Lb: A Super-Neptune-mass Planet Orbiting a Sun-like Host Star, AJ, 157, 72
- Jung, Y. K., Gould, A., & Udalski, A., et al. 2019b, Spitzer Parallax of OGLE-2018-BLG-0596: A Low-mass-ratio Planet around an M-dwarf, AJ, 158, 28
- Kervella, P., Thévenin, F., Di Folco, E., & Ségransan, D. 2004, The angular sizes of dwarf stars and subgiants. Surface brightness relations calibrated by interferometry, A&A, 426, 297
- Kim, S.-L., Lee, C.-U., Park, B.-G., et al. 2016, Three-Site Photometric Monitoring of the Sct-Type Pulsating Star V1162 Orionis: Period Change and its Implications for Pre-Main Sequence Evolution, JKAS, 49, 37
- Kim, D.-J., Kim, H.-W., Hwang, K.-H., et al., 2018a, Korea Microlensing Telescope Network Microlensing Events from 2015: Event-finding Algorithm, Vetting, and Photometry, AJ, 155, 76
- Kim, H.-W., Hwang, K.-H., Kim, D.-J., et al., 2018b, The KMTNet/K2-C9 (Kepler) Data Release, AJ, 155, 186
- Kim, H.-W., Hwang, K.-H., Kim, D.-J., et al., 2018c, The KMTNet 2016 Data Release, arXiv:1804.03352
- Kim, H.-W., Hwang, K.-H., Shvartzvald, et al. 2018d, The Korea Microlensing Telescope Network (KMTNet) Alert Algorithm and Alert System, arXiv:1806.07545
- Minniti, D., Lucas, P., VVV Team, 2017, VizieR Online Data Catalog: VISTA Variable in the Via Lactea Survey DR2 (Minniti+, 2017), yCAT 2348, 0
- Nataf, D.M., Gould, A., Fouqué, P. et al. 2013, Reddening and Extinction Toward the Galactic Bulge from OGLE-III: The Inner Milky Way’s $R_V \sim 2.5$ Extinction Curve, ApJ, 769, 88
- Paczynski, B. 1986, Gravitational microlensing by the galactic halo, ApJ, 304, 1
- Refsdal, S. 1966, On the possibility of determining the distances and masses of stars from the gravitational lens effect, MNRAS, 134, 315
- Ryu, Y.-H., Yee, J.C., Udalski, A., et al. 2017b, OGLE-2016-BLG-1190Lb: First *Spitzer* Bulge Planet Lies Near the Planet/Brown-Dwarf Boundary, AJ, 155, 40
- Ryu, Y.-H., Navarro, M.G., Gould, A. et al. 2019a, KMT-2018-BLG-1292: A Super-Jovian Microlens Planet in the Galactic Plane, AAS submitted, arXiv:1905.04870
- Ryu, Y.-H., Udalski, A., Yee, J.C. et al. 2019b, OGLE-2018-BLG-0532Lb: Cold Neptune With Possible Jovian Sibling, AAS submitted, arXiv:1905.08148
- Schechter, P.L., Mateo, M., & Saha, A. 1993, DOPHOT, a CCD photometry program: Description and tests, PASP, 105, 1342
- Shin, I.-G., Udalski, A., Yee, J.C., et al. 2018, OGLE-2016-BLG-1045: A Test of Cheap Space-based Microlens Parallaxes, ApJ, 863, 23
- Shvartzvald, Y., Yee, J.C., Calchi Novati, S. et al. 2017b, An Earth-mass Planet in a 1 au Orbit around an Ultracool Dwarf, ApJL, 840, L3
- Skowron, J., Udalski, A., Gould, A. et al. 2011, Binary Microlensing Event OGLE-2009-BLG-020 Gives Verifiable Mass, Distance, and Orbit Predictions, ApJ, 738, 87
- Smith, M., Mao, S., & Paczyński, B., 2003, Acceleration and parallax effects in gravitational microlensing, MNRAS, 339, 925
- Street, R., Udalski, A., Calchi Novati, S. et al. 2016, Spitzer Parallax of OGLE-2015-BLG-0966: A Cold Neptune in the Galactic Disk, ApJ, 829, 93.
- Suzuki, D., Bennett, D.P., Sumi, T., et al. 2016, The Exoplanet Mass-ratio Function from the MOA-II Survey: Discovery of a Break and Likely Peak at a Neptune Mass, ApJ, 833, 145
- Udalski, A. 2003, The Optical Gravitational Lensing Experiment. Real Time Data Analysis Systems in the OGLE-III Survey, Acta Astron., Acta Astron., 53, 291
- Udalski, A., Szymanski, M., Kaluzny, J., Kubiak, M., Mateo, M., Krzeminski, W., & Paczyński, B. 1994, The Optical Gravitational Lensing Experiment. The Early Warning System: Real Time Microlensing, Acta Astron., Acta Astron., 44, 227
- Udalski, A., Yee, J.C., Gould, A., et al. 2015a, Spitzer as a Microlens Parallax Satellite: Mass Measurement for the OGLE-2014-BLG-0124L Planet and its Host Star, ApJ, 799, 237
- Udalski, A., Szymański, M.K. & Szymański, G. 2015b, OGLE-IV: Fourth Phase of the Optical Gravitational Lensing Experiment, Acta Astronom., 65, 1
- Udalski, A., Ryu, Y.-H., Sajadian, S., et al. 2018, OGLE-2017-BLG-1434Lb: Eighth $q < 1 \times 10^{-4}$ Mass-Ratio Microlens Planet Confirms Turnover in Planet Mass-Ratio Function, Acta Astron., 68, 1
- Woźniak, P. R. 2000, Difference Image Analysis of the OGLE-II Bulge Data. I. The Method, Acta Astron., 50, 421

- Yee, J.C., Gould, A., Beichman, C., 2015, Criteria for Sample Selection to Maximize Planet Sensitivity and Yield from Space-Based Microlens Parallax Surveys, *ApJ*, 810, 155
- Yoo, J., DePoy, D.L., Gal-Yam, A. et al. 2004, OGLE-2003-BLG-262: Finite-Source Effects from a Point-Mass Lens, *ApJ*, 603, 139